

# *Suzaku* Observation of the High-Inclination Binary EXO 0748–676 in the Hard State

Zhongli Zhang<sup>1,2</sup>, Soki Sakurai<sup>1</sup>, Kazuo Makishima<sup>1,3,4</sup>, Kazuhiro Nakazawa<sup>1,4</sup>, Ko Ono<sup>1</sup>, Shin’ya Yamada<sup>5</sup>, and Haiguang Xu<sup>6,7</sup>

## ABSTRACT

Utilizing an archived *Suzaku* data acquired on 2007 December 25 for 46 ks, X-ray spectroscopic properties of the dipping and eclipsing low-mass X-ray binary EXO 0748–676 were studied. At an assumed distance of 7.1 kpc, the data gave a persistent unabsorbed luminosity of  $3.4 \times 10^{36}$  erg cm<sup>-2</sup> s<sup>-1</sup> in 0.6 – 55 keV. The source was in a relatively bright low/hard state, wherein the 0.6 – 55 keV spectrum can be successfully explained by a “double-seed” Comptonization model, incorporating a common corona with an electron temperature of  $\sim 13$  keV. The seed photons are thought to be supplied from both the neutron star surface, and a cooler truncated disk. Compared to a sample of non-dipping low-mass X-ray binaries in the low/hard state, the spectrum is subject to stronger Comptonization, with a relatively larger Comptonizing  $y$ -parameter of  $\sim 1.4$  and a larger coronal optical depth of  $\sim 5$ . This result, when attributed to the high inclination of EXO 0748–676, suggests that the Comptonizing corona may elongate along the disk plane, and give a longer path for the seed photons when viewed from edge-on inclinations.

*Subject headings:* accretion, accretion disks – Stars: neutron – X-rays: binaries – radiative transfer

---

<sup>1</sup>Department of Physics, School of Science, The University of Tokyo, 7-3-1, Hongo, Bunkyo-ku, Tokyo 113-0033, Japan; e-mail: zzhang@juno.phys.s.u-tokyo.ac.jp

<sup>2</sup>Shanghai Astronomical Observatory, Chinese Academy of Sciences, 80 Nandan Road, 200030 Shanghai, PR China

<sup>3</sup>MAXI Team, Institute of Physical and Chemical Research (RIKEN), Wako, Saitama 351-0198, Japan

<sup>4</sup>Research Center for the Early Universe, The University of Tokyo, 7-3-1, Hongo, Bunkyo-ku, Tokyo 113-0033, Japan

<sup>5</sup>Department of Physics, Tokyo Metropolitan University, Minami-Osawa 1-1, Hachioji-shi, Tokyo 192-0397, Japan

<sup>6</sup>Department of Physics and Astronomy, Shanghai Jiao Tong University, 800 Dongchuan Road, Minhang, Shanghai 200240, China

<sup>7</sup>IFSA Collaborative Innovation Center, Shanghai Jiao Tong University, 800 Dongchuan Road, Minhang, Shanghai 200240, China

## 1. Introduction

Neutron-star low-mass X-ray binaries (hereafter LMXBs), luminous X-ray objects in the Milky Way and other galaxies, are low-magnetic-field neutron stars (NSs) accreting materials from their low-mass companions through Roche lobe overflow. They are found either in the high/soft state (HSS) or the low/hard state (LHS) (e.g., White & Mason 1985; Mitsuda et al. 1984, 1989). For “atoll” sources including the LMXBs studied in the present paper, these physical states correspond respectively to the “banana” and “island” states (Hasinger & van der Klis 1989), which are based on empirical color-color diagrams. In the LHS, an LMXB exhibits a rather hard spectrum extending to  $\sim 100$  keV, which is considered to arise from thermal Comptonization, wherein some soft photons are boosted to higher energies by hot electrons (Sunyaev & Titarchuk 1980) in a vicinity of the NS. The cloud of hot electrons is often referred to as “Comptonizing corona” (hereafter CC; Chapline & Stevens 1973; Lamb & Sanford 1979).

Generally, the CC is identified as a geometrically thick and optically thin accretion flow, which is considered to form near an accreting compact object when the mass accretion rate is relatively low (Lightman & Eardley 1974). Recent *Suzaku* observations (e.g., Sakurai et al. 2012, 2014) are confirming that the CC in several LMXBs is accreting relatively isotropically onto the NS, at least when the luminosity is  $\sim 1\%$  of the Eddington luminosity ( $L_{\text{edd}}$ ; Matsuoka & Asai 2013; Sakurai et al. 2014). However, the more detailed geometry of the inflowing corona is still unclear. In particular, it is still unknown whether it is very spherical, or oblate towards the disk plane. Thus we are motivated to compare “dipping” and “non-dipping” LMXBs in the LHS, in order to further study the coronal shape.

Dipping LMXBs, or “dippers”, are characterized by periodic dips in their X-ray intensity, and are considered to be intrinsically the same as non-dipping LMXBs, except for their more edge-on inclination angles. If CC has an oblate shape, dipping LMXBs would show systematically stronger Comptonization in the non-dipping period, because the seed photons must pass through the CC with a longer path. Indeed, dippers have been reported to exhibit rather hard X-ray spectra over a large range of luminosity. Examples include *BeppoSAX* observations of 4U 1915–05 (Church et al. 1998), XB 1254–690 (Iaria et al. 2001), XB 1323–619 (Bałucińska-Church et al. 1999) and EXO 0748–676 (Sidoli et al. 2005).

In these previous studies of dipping LMXBs, the X-ray spectra were in most cases fitted with an empirical cutoff power-law model. However, this is not physical, and does not enable detailed comparison between dippers and other LMXBs. Given this, Zhang et al. (2014) studied a *Suzaku* data set of 4U 1915–05 in the HSS. They successfully reproduced the 0.8 – 45 keV spectrum of this source, using the canonical two component spectral model (Mitsuda et al. 1984) that describes broadband X-ray spectra of non-dipping LMXBs in the HSS. Furthermore, they found that the blackbody component of this dipper is more strongly Comptonized than in nor-

mal LMXBs. This gives evidence that the CC in the HSS is rather flattened to the accretion disk plane, in agreement with the report by Gladstone et al. (2007), that dipping LMXBs in the HSS have systematically harder spectra than normal LMXBs. In the LHS, however, evidence of flattened coronae has so far been obtained only in black hole binaries (BHBs, e.g., Makishima 2007; Heil et al. 2015). So, in the present paper, we intend to carry out similar studies for LMXBs in the LHS.

For the above purpose, we again choose the Japanese satellite *Suzaku* (Mitsuda et al. 2007), which possesses both a high energy resolution and a broadband coverage. Among the four LHS dipping LMXBs (EXO 0748–676, XB 1323–619, XTE J1710–281 and 4U 1822–37) in *suzaku* archive, we selected EXO 0748–676, which has the highest X-ray flux as indicated in Table 1 of Zhang et al. (2014). From an *EXOSAT* observation, Parmar et al. (1986) first discovered that EXO 0748–676 shows irregular intensity dips and a total eclipse, synchronized with its orbital period of 3.82 hr, and constrained the source inclination angle to be  $i = 75^\circ - 83^\circ$ . We hence fix  $i = 80^\circ$  in the present paper. Since then, the object has been studied by many authors, including Cottam et al. (2001), Jimenez-Garate et al. (2003), Sidoli et al. (2005) and Díaz Trigo et al. (2011). However, except for Sidoli et al. (2005), most of these publications focused on the dip phenomenon or X-ray bursts, without much attention to the intrinsic persistent emission. In the present work, we utilize the *Suzaku* observation of this source, in order to obtain physical constrains on the source accretion scheme (section 5.1), including the shape of the CC (from section 5.2).

In the present paper, we employ a source distance of  $d = 7.1 \pm 1.2$  kpc, which is based on the detailed analysis of helium-dominated X-ray bursts with photospheric radius expansion (Galloway et al. 2008). This value is consistent with an upper limit from analysis of persistent spectra by Díaz Trigo et al. (2011), but is larger than is indicated by the X-ray burst analysis assuming hydrogen-dominated atmosphere ( $d \sim 5$  kpc, Wolff et al. 2005; Galloway et al. 2008). Thus, we include a distance uncertainty of 30%.

## 2. Observation

EXO 0748–676 was observed by *Suzaku* on 2007 December 25 (MJD 54459) with ObsID of 402092010. The observation started at 05:41:13, and ended at 07:00:24 the next day with an elapsed time of 91.0 ks and a net exposure time of 45.9 ks. The soft X-ray band (0.2 – 12 keV) was covered by three cameras of the X-ray Imaging Spectrometer (XIS 0, XIS 1 and XIS 3) on board, while XIS 2 had stopped working before this observation. We utilized only XIS 0 and XIS 3 to extract light curves (section 2.2) and spectrum (section 3), because these front-illuminated CCD cameras are more accurately calibrated than XIS 1 which uses a back-illuminated CCD chip. In the hard X-ray band above 10 keV, we analyzed HXD-PIN data which have an energy coverage up

to 70 keV. The data from HXD-GSO were not employed because the source was not significantly detected therein. Both the XIS and HXD-PIN data were analyzed by HEASoft version 6.13, with the calibration database of version 20070731 for the XIS, and version 20070710 for the HXD.

## 2.1. XIS and HXD-PIN Data Analysis

In the present observation, XIS 0 and XIS 3 were both operated in the normal mode using 1/4 window option. For each CCD camera, events with pixel formats of  $3 \times 3$  and  $5 \times 5$  were combined, and the events with grades 0,2,3,4 and 6 were selected. The total count rate was  $\sim 11.0$  cts  $s^{-1}$  per XIS camera. With a time resolution of 2 s, photon pileup is negligible (Yamada et al. 2012). Thus, around the X-ray center at  $\alpha = 07^h48^m31.19^s$  and  $\delta = -67^\circ45'09.52''$  (J2000.0), we accumulated on-source events over a circle of  $2'$ , which contains 90% of the source counts. The background regions were chosen to be two circles from two edges of the CCD, each located  $7'$  from the source center, with a radius of  $1'.4$ ; the total background area equals to the source area. The background-subtracted source count rate in the  $0.6 - 10$  keV range is  $9.33 \pm 0.01$  cts  $s^{-1}$ , when averaged between XIS 0 and XIS 3.

The source was detected up to 55 keV with HXD-PIN. The raw  $12 - 55$  keV count rate was  $1.06 \pm 0.01$  cts  $s^{-1}$  on average, among which  $0.54$  cts  $s^{-1}$  was Non X-ray Background (NXB) according to the NXB model provided by the HXD team. Contribution from the Cosmic X-ray Background (CXB) was calculated to be  $0.02$  cts  $s^{-1}$  using a model as

$$CXB(E) = 9.41 \times 10^{-3} \left( \frac{E}{1 \text{ keV}} \right)^{1.29} \exp \left( -\frac{E}{40 \text{ keV}} \right) \quad (1)$$

(Boldt 1987), where the unit is photons  $\text{cm}^{-2} \text{ s}^{-1} \text{ keV}^{-1} \text{ FOV}^{-1}$ . After subtracting both NXB and CXB, and further correcting the data for the dead time with a command `hxddtcor`, the  $12 - 55$  keV PIN signal count rate became  $0.58 \pm 0.01$  cts  $s^{-1}$ .

## 2.2. Light Curves

Figure 1 (left panels) shows background-subtracted (using `lcmath`) light curves of the XIS and HXD-PIN, and the ratio of the latter to the former. From the HXD-PIN data we subtracted only the NXB, since the CXB is constant and rather minor. Multiple dips are seen in the light curves, especially in that of the XIS, as repeatedly reported and explained to be caused by an ionized absorber on the accretion disk (Díaz Trigo et al. 2006). Four type I X-ray bursts were also detected at observation times of 30.0 ks, 47.0 ks, 64.6 ks and 85.7 ks. Detailed analysis of the

dips and bursts are out of the scope of this paper. Except for the dips and bursts, both the XIS and HXD-PIN count rates, and hence the hardness ratio, remained constant within  $\sim 10\%$ .

After excluding the bursts, we folded the XIS and HXD-PIN light curves and the hardness ratio at the orbital period of  $P_{\text{orb}} = 13766.8$  s measured by Parmar et al. (1986). Phase 0 (=1) was set to be the middle of the eclipse, which refers to 06:12:03 of 2007 December 25 (MJD = 54459.26018). The results are shown in the right panels of figure 1. The dips (except for the eclipses) are noticed only in the XIS light curve over an orbital phase  $\phi \sim 0.6 - 1.1$ , while the rest can be considered as non-dip phases.

### 3. Analysis of Non-Dip Spectra

#### 3.1. Preparation of Spectra

Since the XIS and HXD-PIN light curves are both approximately constant (figure 1), we utilized the whole observation period for the non-dip spectral analysis, but excluding the orbital phases of  $\phi = 0.6 - 1.1$  in reference to figure 1. The type I X-ray bursts (with the 0.6-10 keV XIS count rate  $> 12$  cts  $\text{s}^{-1}$ ) were also removed. By further requiring the simultaneous presence of the XIS and HXD-PIN data, the remaining exposure became 16.2 ks, which is  $\sim 35\%$  of the total exposure. Spectra from XIS 0 and XIS 3 were co-added; so were their responses. To analyze the HXD-PIN data, we utilized the “XIS nominal” response file released from the HXD team, and the CXB contribution was included in a model as a fixed component of equation (1). We chose an energy range of 0.6 – 10 keV for the XIS, and 12 – 55 keV for the HXD-PIN data. To avoid the calibration uncertainties around the instrumental silicon K-edge and the gold M-edge, we excluded 1.7 – 1.9 keV and 2.2 – 2.4 keV energy ranges of the XIS spectrum, respectively. The instrumental Al K-edge, which is not fully accounted for by the response, was fitted by an edge model, with the edge energy fixed at 1.56 keV. The cross normalization of HXD-PIN relative to the XIS was fixed at 1.158 (Kokubun et al. 2007).

Figure 2(a) shows the derived count spectrum, and figure 2(b) shows its  $\nu F_\nu$  form. Thus, the spectrum extends up to  $\sim 20$  keV with a hard slope, and then turns over gradually. It can be approximated (with  $\chi^2/\nu = 295.6/142$ ) by the model `highecut*powerlaw`, defined as

$$A(E) = \begin{cases} KE^{-\Gamma} \exp[(E_c - E)/E_f] & (E \geq E_c) \\ KE^{-\Gamma} & (E \leq E_c) \end{cases}, \quad (2)$$

with a photon index  $\Gamma \sim 1.7$ , a cutoff energy  $E_c \sim 22$  keV, and an e-folding energy  $E_f \sim 60$  keV, while  $K$  is the normalization. The low  $\Gamma$  value indicates that the source was in the LHS with strong

Comptonization, while the value of  $E_c$  suggests a relatively low coronal electron temperature. The data-to-model ratio in panel (c) reveals a soft excess below  $\sim 1$  keV, which suggests that the overall emission may contain more than a single component.

### 3.2. Single-Seed Comptonization Models

Although the empirical model in figure 2 is roughly successful, it is not yet fully acceptable, and it has little physical meaning. Hence, we attempt to fit the spectrum with the canonical two-component spectral model for LMXBs, `diskbb+bbbody` (Mitsuda et al. 1984), applying the Comptonization code `nthcomp` (Zdziarski et al. 1996; Życki et al. 1999) on either (single-seed) or both (double-seed) of the two optically-thick components. In Sakurai et al. (2012), the model `diskbb+nthcomp[bbbody]`, in which the seed photons are from the NS surface as indicated by the square bracket, successfully explained the LHS spectra of Aql X–1 obtained with *Suzaku*. Thus, we first applied the same model to the spectra of EXO 0748–676. Column density of photoelectric absorption was fixed to the Galactic line-of-sight value of  $N_H = 1.1 \times 10^{21} \text{ cm}^{-2}$ , because the source locates  $\sim 2.4$  kpc below the Galactic plane, as calculated from its Galactic latitude  $b = -19.8^\circ$ , and the source distance of 7.1 kpc; hence, the source is outside the neutral hydrogen disk of the Galaxy.

The obtained results are shown in figure 3(a). Around  $0.8 - 1.2$  keV, we noticed some negative residual features that cannot be explained by the Galactic absorption, with the fit goodness of  $\chi^2(\nu) = 175.0$  (142). Thus we added a partial ionized absorber with the code `zxipcf` in XSPEC, using a grid of XSTAR photoionized absorption models (Reeves et al. 2008). The absorber column density  $N_{\text{abs}}$ , the ionization parameter  $\log(\xi)$ , and the absorber covering fraction were set to be free, while the redshift was fixed to 0. The fit gave  $N_{\text{abs}} < 1.1 \times 10^{22} \text{ cm}^{-2}$  and  $\log(\xi) \sim 2.4$ , together with  $\chi^2(\nu) = 166.5$  (139). However, as shown in figure 3(b), an absorption feature was still evident at  $\sim 1$  keV, which may be related to Neon  $\text{Ly}\alpha_1$ . We hence added a Gaussian absorption model, with the  $1\sigma$  line width fixed at 20 eV.

Through the above improvements, the fit has become fully acceptable with  $\chi^2(\nu) = 142.8$ (137), as shown in table 1 labeled as “single-seed” model, and in figure 3(c). The obtained inner-disk temperature  $kT_{\text{in}} \sim 0.2$  keV and the radius  $R_{\text{in}} \sim 160$  km indicate a disk truncated at a large radius. For the NS blackbody, which serves as the seed component of the `nthcomp` model, the data gave only an upper limit of  $kT_{\text{bb}} \sim 0.25$  keV, and a lower limit of  $R_{\text{bb}} \sim 33$  km as specified by the `nthcomp` normalization. However, this value of  $R_{\text{bb}}$  is much larger than the neutron star radius, even considering the 30% distance uncertainty. This means that the data requires more seed photons than are available from the NS surface, encouraging us to consider a “double-seed” modeling in the next subsection.



In addition to the above attempts, we also considered two more single-seed Comptonization models. One is `bbody+nthcomp[diskbb]`, assuming that the seed photons are supplied only from the disk. This is equivalent to some disk Comptonization models (e.g., Church & Balucinska-Church 1995). The other is a partial NS Comptonization model, `bbody+nthcomp[bbody]`, in which some fraction of the NS blackbody is Comptonized while the rest is directly visible, and the disk emission is not detected. Both models gave acceptable fits to the data; however, neither of them was physically acceptable. The disk Comptonization model gave too large a blackbody radius as  $R_{\text{bb}} > 100$  km, trying to explain the soft excess with a rather low temperature, and too large a disk radius as  $R_{\text{in}} > 1000$  km to supply a sufficient number of seed photons. In the partial NS Comptonization model, the directly seen `bbody` component and the Comptonized seed `bbody` both became too large in radius as  $R_{\text{bb}} > 100$  km, for a similar reason as above. Thus, we no longer consider these two models hereafter.

We further examined the spectrum for the possible presence of other additional components, especially a directly seen NS blackbody emission (e.g., Lyu et al. 2014), and disk reflection (e.g., Di Salvo et al. 2015). By adding another `bbody` component to our final single-seed solution (figure 3c), the fit was improved by  $\Delta\chi^2 = -7.46$  for  $\Delta\nu = -2$ . The derived blackbody temperature is  $0.4^{+0.1}_{-0.2}$  keV with a reasonable blackbody radius of  $2.9^{+8.0}_{-0.9}$  km. However, the Comptonized `bbody` component did not change significantly, so that the total blackbody radius further increased and hence the fit became even more unphysical. For the disk reflection, we multiplied a `reflect` component on our model and derived a scaling factor (the solid angle divided by  $2\pi$ ) of  $\sim 0.16$ . However, the fit was improved only by  $\Delta\chi^2 = -0.9$  for  $\Delta\nu = -1$ ; thus we do not consider that a reflection component is very necessary in this high inclination system.

### 3.3. Double-Seed Comptonization Models

In order to overcome the seed-photon shortage revealed in section 3.2, we next consider a “double-seed” Comptonization, namely, the case wherein the disk emission and the NS blackbody are both Comptonized to jointly produce the hard continuum. The model thus becomes `nthcomp[diskbb]+nthcomp[bbody]` with the common Galactic absorption. The values of  $kT_e$  and  $\Gamma$  were first constrained to be the same between the two Comptonization components, but the fit was far from acceptable since the model could not explain the slightly concave spectral shape. As indicated by recent results on LMXBs in the LHS (e.g., Sakurai et al. 2014), the disk is likely to be truncated at a large distance from the central NS, and hence it is reasonable to assume different optical depths for the two Comptonization components. Hence, we allowed them to have different values of  $\Gamma$ , while  $kT_e$  was kept the same. This model was found to be successful with  $\chi^2(\nu) = 134.6$  (136). Compared to the single-seed model, it is better by  $\Delta\chi^2 = -6.5$ , for a decrease of only

by  $\Delta\nu = -1$ .

The successful fit obtained above is shown in table 1 as “double-seed” model, and in figure 3(d). Thus, the Comptonized disk emission takes a larger fraction of the soft-band emission below 2 keV, compared to the solution of the single-seed model. As a result, the NS component moved to higher energies with a higher  $kT_{\text{bb}}$  and a considerably smaller  $R_{\text{bb}}$  which is physically acceptable within errors. This solves the problem encountered in the single-seed modeling. The value of  $R_{\text{in}}$  has become even larger than that obtained in the single-seed modeling, but its lower limit is still reasonable at  $\sim 150$  km, calculated using the lower limit on the distance (5 kpc, Galloway et al. 2008) and the upper limit on the inclination ( $75^\circ$ , Parmar et al. 1986). The coronal temperature has remained relatively unchanged from the single-seed model. The slope  $\Gamma$  for the disk has been found to be much larger (steeper) than that for the NS, resulting in a  $\sim 5$  times smaller coronal optical depth (table 1). This is reasonable considering the large value of  $R_{\text{in}}$ . We further allowed the two Comptonized components to have different values of  $kT_e$ . Then, the disk component favored a lower value of  $kT_e$ , but the fit goodness did not change significantly.

Based on this modeling, the unabsorbed source flux in 0.6 – 55 keV was calculated to be  $5.7 \times 10^{-10}$  erg cm $^{-2}$  s $^{-1}$ , which gives an unabsorbed luminosity of  $3.4 \times 10^{36}$  erg cm $^{-2}$  s $^{-1}$  in 0.6 – 55 keV and  $5.2 \times 10^{36}$  erg cm $^{-2}$  s $^{-1}$  after bolometric correction. The latter corresponds to  $\sim 0.025 L_{\text{edd}}$  assuming a hydrogen-dominated donor star. The luminosity could be twice higher if we considered the inclination effect, or lower by a factor of 2 if taking into account the 30% distance uncertainty.

#### 4. *Suzaku* Archived Sample of Non-dipping LMXBs

So far, we have successfully explained the *Suzaku* spectra of EXO 0748–676 using a spectral model that was developed to explain those of non-dipping LMXBs in the LHS. The next task is to examine whether the derived model parameters, in particular  $\tau$  and  $kT_e$ , differ between the present dipping source and other non-dipping ones. For this purpose, we performed, after Sakurai (2015), a survey of “normal” LMXB spectra in the *Suzaku* archive. In addition to dippers, we also excluded high magnetic field sources (e.g., Her X–1, GX 1+4, 4U 1626–67, and 4U 1822–37; Sasano et al. 2014), ultra compact X-ray binaries (with hydrogen-depleted donor stars), and symbiotic binaries (with evolved companions), because the accreting matters in the latter two types of systems are considered to have non-solar electron-to-baryon number ratios, which may affect the Comptonization details. As listed in Table 2, this selection left us with 43 observations of 16 normal LMXBs. As shown by Sakurai (2015), the hardness ratio  $H$  between the 20 – 40 keV HXD-PIN signal rates to the 5 – 10 keV XIS-FI signal rates (both with the background subtracted) serves as a good state indicator. Thus, 16 observations of 8 sources were found to sample the LHS, with  $H > 0.03$ ;



these are listed in Table 3. Among them, the six observations of Aql X–1 (ObsID from 402053020 to 402053070) were previously analyzed by Sakurai et al. (2014) and were updated by Sakurai (2015). Besides, GS 1826–238 was further studied in detail by Ono et al. (2016), of which the results are quoted in the present paper.

We analyzed the data of the remaining 15 observations employed similar procedures as described in section 2.1. A major difference is that the XIS background events were taken from an annulus with the inner radius of  $4'$  and the outer radius of  $5'$ . Moreover, the emission from Aql X–1 was detected with HXD-GSO up to  $> 100$  keV.

We then fit the spectra of the XIS and the HXD jointly, using either the single-seed or the double-seed models employed in the previous section. As for the Comptonization code, either `nthcomp` or `compPS` (Poutanen & Svensson 1996) was adopted when the optical depth is  $\tau \gtrsim 2$  or  $\tau \lesssim 2$ , respectively. The latter model was employed under spherical geometry, namely the geometry parameter of 4 in XSPEC. In an overlapping parameter region at  $\tau \sim 2$ , the two codes yielded very similar  $kT_e$  and  $\tau$  within  $\sim 3\%$  (Sakurai 2015). Since these LHS sources span a large range ( $\sim 5$  orders of magnitude) of luminosities (or mass accretion rates), their spectra exhibited some variety. For example, the disk emission was undetectable from the two faintest sources, Cen X–4 and SLX 1737–282, and the three faintest observations of Aql X–1. Twelve out of the 15 spectra were explained by the single-seed modeling (section 3.2), while the remaining three (two from 4U 1705–44, and one from Aql X–1) required the double-seed modeling. However, unlike EXO 0748–676, these data sets preferred a common corona with the same  $kT_e$  and  $\tau$  for the two-seed sources. The disk reflection was found to be necessary only for three observations of Aql X–1 (ObsID from 402053020 to 402053040), as already published in Sakurai et al. (2012). The fit results to the 15 spectra are summarized in Table 3. We discuss these results in section 5.

## 5. Discussion and Conclusion

### 5.1. The Spectral Modeling of EXO 0748–676

During the present *Suzaku* observation, EXO 0748–676 was in the LHS because it exhibited a very hard spectral slope of  $\Gamma \sim 1.7$  up to  $\sim 20$  keV (figure 2). This classification is also supported by its high value of the hardness ratio (section 4),  $H = 0.077 \pm 0.002$ . Its persistent luminosity,  $L_{\text{bol}} \sim 0.025^{+0.025}_{-0.013} L_{\text{edd}}$ , is relatively high among LMXBs in the LHS, considering that the soft-to-hard state transition luminosity for LMXBs is generally  $0.01 - 0.04 L_{\text{edd}}$  (Maccarone 2003; Matsuoka & Asai 2013). Such a luminous hard-state LMXB is however not rare, as the luminosity range of the *Suzaku* LHS sample spans from  $\lesssim 0.01$  to  $\sim 0.1 L_{\text{edd}}$  (Table 3).

The broadband *Suzaku* spectrum of this object has been described successfully with the canon-

ical two-component model for LMXBs (Mitsuda et al. 1984), namely, the NS and disk emissions, plus Comptonization. The data indicate a “double-seed” Comptonization condition (sections 3.2 and 3.3), where the NS blackbody emission and the disk emission are both Comptonized, to form the hard continuum and to acquire a higher color temperature, respectively. Assuming a common electron temperature, the obtained value of  $kT_e \sim 13$  keV is relatively low for LMXBs in the LHS, as judged from the compilation in Table 3, where most of the other sources show  $kT_e > 20$  keV. The optical depths of the two components were calculated using equation (2) of Zhang et al. (2014), so were the Comptonizing  $y$ -parameters defined therein. As clearly seen in figure 3(d), the disk component is less Comptonized than the NS component, because the corresponding disk/NS ratio of  $\tau$  is  $\sim 1/5$ , and the ratio of  $y$ -parameters is  $\sim 1/10$ . Considering the large value of  $R_{in}$ , it suggests that the corona is centrally localized, and the disk intrudes into only the outer part of the corona. Similar results were obtained by Ono et al. (2016) on GS 1826–238, that only an inner region of a truncated accretion disk is Comptonized.

We further compared the above results with the compilation of the *Suzaku* sample shown in Table 3. There, the fit results to the 16 LHS spectra of the 8 LMXBs can be classified into three categories, based on their best-fit models; while these categories all involve Comptonized NS emission, their difference is in the disk emission. The five observations in category 1 (C1) did not have disk emission detected in the *Suzaku* spectra, and their luminosities are all  $< 0.01L_{edd}$ . In seven observations with  $L_X \gtrsim 0.01L_{edd}$ , forming category 2 (C2), the disk was detected but it did not need to be Comptonized. Finally, in the four most luminous observations with  $L_X \sim 0.1L_{edd}$ , to be called category 3 (C3), the disk emission was also strongly Comptonized by a corona that can be considered either to be the same (with the same  $kT_e$  and  $\tau$  values) as for the NS Comptonization (406010010 of Aql X–1 and 4U 1705–44), or to have a lower temperature (GS 1826–238; Ono et al. 2016). The luminosity of EXO 0748–676 is higher than in most of the LMXBs in C2, and lower than (ignoring the inclination effect) in all LMXBs in C3. The accretion scheme of this source is likely in between those of LMXBs with single-seed and double-seed Comptonization, because the fit prefers disk Comptonization, but to a less extent than that of the NS.

Further comparing the results on EXO 0748–676 (Table 1) with those of the other LMXBs (Table 3), two possible differences are noticed; the considerably larger value of  $R_{in}$ , and the somewhat lower  $kT_{bb}$  ( $\lesssim 0.4$  keV vs.  $\gtrsim 0.5$  keV). However, we consider these to be still within systematic uncertainties of the spectral modeling, for the following reasons. First, the disk emission of EXO 0748–676 is very much weakened by the high inclination, and couples strongly with the neutral and ionized absorptions at the softest end of the spectrum. As a result, the  $diskbb$  and its Comptonization must be subject to considerable systematic uncertainties. Second, in figure 3(d), the value of  $kT_{bb}$  is constrained only by the 1–2 keV data points, where the Rayleigh-Jeans regime of the underlying blackbody is directly visible. Since this is the very energy range where the disk emission and the Comptonized blackbody overlap, the systematic uncertainties will propagate

from the former to the latter. To test the above inferences, we re-fitted the EXO 0748–676 spectra with the same model as in figure 3(d), but fixing  $kT_{\text{bb}}$  at 0.5 keV. Then, the fit goodness decreased only slightly, by  $\Delta\chi^2 = 16.2$  for  $\Delta\nu = +1$ . Therefore, we do not consider that the model parameters of EXO 0748–676 are deviated from those of the other objects.

## 5.2. Properties of the Comptonizing Corona

Now we discuss the Comptonizing effects of EXO 0748–676. Judging directly from the spectral shape, EXO 0748–676 exhibited a hard spectral slope of  $\Gamma = 1.7$  in 5 – 20 keV, an energy band dominated by the Comptonized NS emission and is free from interstellar absorption. It could be even harder as once revealed by *BeppoSAX* in 2000, wherein the spectrum extended to  $\sim 100$  keV with  $\Gamma \sim 1.3$  (Sidoli et al. 2005). Other non-dipping LHS LMXBs, in contrast, show a rather flat slope in  $\nu F_\nu$  plot of  $\Gamma \sim 2$  in the same energy range. Examples in the literatures include the persistent LMXBs in the LHS, GS 1826–238 (figure 2 of Ono et al. 2016), 4U 1728–34 (figure 6 of Tarana et al. 2011), 4U 1705–44 (top panel in figure 3 of Lin et al. 2010) and 4U 1812–12 (figure 2 of Tarana et al. 2006), and the transient LMXBs in the LHS, Aql X–1 (figure 2 of Sakurai et al. 2014) and 4U 1608–522 (top left panel in figure 5 of Tarana et al. 2008). The harder spectral slope indicates that EXO 0748–676 has stronger Comptonization of the NS component than the others.

Let us more quantitatively compare EXO 0748–676 with the *Suzaku* sample. For this purpose, figure 4(a) shows the calculated Compton  $y$ -parameter of the present sources, including EXO 0748–676, against their bolometric luminosity  $L_X$ . From the low luminosity end, the  $y$ -parameter remains approximately constant at  $\sim 0.5$  within errors till  $2 - 4 \times 10^{36}$  erg s $^{-1}$ , and then increases towards higher luminosities. The point of EXO 0748–676, plotted in diamond, is an obvious outlier with a  $\sim 1.5 - 3$  times higher  $y$  value than sources with similar  $L_X$ . This confirms that the NS emission is more strongly Comptonized in EXO 0748–676 than in the other sources. Furthermore, this effect must be attributed to a larger  $\tau$  of EXO 0748–676, because it has a rather low  $kT_e$ . Indeed, this expectation is directly confirmed in an  $L_X$ - $\tau$  plot presented in figure 4(b), where EXO 0748–676 again stands out.

Although the luminosity is the primary quantity to control the behavior of LMXBs, it is subject to distance (and some extent inclination) uncertainties. Moreover, a hysteresis effect (Meyer-Hofmeister et al. 2005; Miyamoto et al. 1995) may complicate the behavior of sources near the transition luminosities, including EXO 0748–676. Hence, we introduce a new parameter  $Q \equiv kT_e/kT_{\text{bb}}$  proposed by Makishima (2014), which represents a balance between the electron heating from ions, and their cooling through Comptonization by the seed photons. This quantity is independent of the source distance, and has been confirmed to be free from the hysteresis. It hence serves as a good state indicator, which separates the HSS ( $Q \lesssim 7$ ) from the LHS ( $Q \gtrsim 10$ )

(Makishima 2014; Sakurai 2015). We show  $Q$ - $y$  and  $Q$ - $\tau$  diagrams in figure 4(c) and figure 4(d), respectively. Thus, the systematically larger  $y$  and  $\tau$  of EXO 0748–676 are still apparent, even when  $L_X$  is replaced by  $Q$ .

Because EXO 0748–676 has a very high inclination compared to the other LMXBs considered here, its large  $\tau$  can be most naturally ascribed to a flattened coronal shape, which will give a longer path length when viewed from high inclinations. As indicated by figure 4(b) and 4(d), the  $\tau$  value of EXO 0748–676 is about twice of the average value of the other LMXBs with the same  $L_X$  and  $Q$ . Assuming that the corona has an axi-symmetric ellipsoidal geometry, that the electron density does not depend significantly on the sources, and that the inclination is  $i = 80^\circ$  in EXO 0748–676 and typically  $\sim 45^\circ$  in the other sources, the higher value of  $\tau$  by a factor of  $\sim 2$  can be explained if the corona has an aspect ratio of  $\sim 3:1$ . Combined with Zhang et al. (2014), who found evidence for a flattened corona in the HSS dipper 4U 1915-05, the present study further suggests that the CC in the LMXBs has an oblate shape in general, although its exact geometry is yet to be quantified.

The present results are very similar to the reported evidence for flattened coronae in BHBs in the LHS by Makishima (2007) and Heil et al. (2015). Especially, Heil et al. (2015) reported that flattened coronae are present in a wide range of hard and intermediate states. In summary, we suggest that the flattened coronal shape is common to LMXBs and BHBs, and to be rather independent of their spectral states.

This work was supported by the Japan Society for the Promotion of Science (JSPS) under the Grant-In-Aid number 24-02321, the Ministry of Science and Technology of China (grant No. 2013CB837900), and the National Science Foundation of China (grant Nos. 11125313 and 11433002).

## REFERENCES

- Barret, D., Olive, J. F., Boirin, L., et al. 2000, *ApJ*, 533, 329
- Barret, D., Olive, J. F., & Oosterbroek, T. 2003, *A&A*, 400, 643
- Bałucińska-Church, M., Church, M. J., Oosterbroek, T., Segreto, A., Morley, R., & Parmar, A. N. 1999, *A&A*, 349, 495
- Boldt, E. 1987, *Observational Cosmology*, 124, 611
- Chevalier, C., Ilovaisky, S. A., van Paradijs, J., Pedersen, H., & van der Klis, M. 1989, *A&A*, 210, 114
- Christian, D. J., & Swank, J. H. 1997, *ApJS*, 109, 177
- Church, M. J., & Balucinska-Church, M. 1995, *A&A*, 300, 441
- Church, M. J., Balucinska-Church, M., Dotani, T., & Asai, K. 1998, *ApJ*, 504, 516
- Cocchi, M., Bazzano, A., Natalucci, L., et al. 2000, *A&A*, 357, 527
- Cornelisse, R., in’t Zand, J. J. M., Verbunt, F., et al. 2003, *A&A*, 405, 1033
- Cottam, J., Kahn, S. M., Brinkman, A. C., den Herder, J. W., & Erd, C. 2001, *A&A*, 365, L277
- Chapline, G., Jr., & Stevens, J. 1973, *ApJ*, 184, 1041
- Díaz Trigo, M., Parmar, A. N., Boirin, L., Méndez, M., & Kaastra, J. S. 2006, *A&A*, 445, 179
- Díaz Trigo, M., Boirin, L., Costantini, E., Méndez, M., & Parmar, A. 2011, *A&A*, 528, A150
- Di Salvo, T., Farinelli, R., Burderi, L., et al. 2002, *A&A*, 386, 535
- Di Salvo, T., Iaria, R., Matranga, M., et al. 2015, *MNRAS*, 449, 2794
- Feast, M. 1999, *New Views of the Magellanic Clouds*, 190, 542
- Fender, R. P., & Hendry, M. A. 2000, *MNRAS*, 317, 1
- Frank, J., King, A. R., & Lasota, J.-P. 1987, *A&A*, 178, 137
- Galloway, D. K., Psaltis, D., Chakrabarty, D., & Muno, M. P. 2003, *ApJ*, 590, 999
- Galloway, D. K., Muno, M. P., Hartman, J. M., Psaltis, D., & Chakrabarty, D. 2008, *ApJS*, 179, 360

- Galloway, D. K., Özel, F., & Psaltis, D. 2008, MNRAS, 387, 268
- Gladstone, J., Done, C., & Gierliński, M. 2007, MNRAS, 378, 13
- Haberl, F., & Titarchuk, L. 1995, A&A, 299, 414
- Hasinger, G., & van der Klis, M. 1989, A&A, 225, 79
- Heil, L. M., Uttley, P., & Klein-Wolt, M. 2015, MNRAS, 448, 3348
- Iaria, R., Di Salvo, T., Burderi, L., & Robba, N. R. 2001, ApJ, 548, 883
- in’t Zand, J. J. M., Verbunt, F., Kuulkers, E., et al. 2002, A&A, 389, L43
- Jimenez-Garate, M. A., Schulz, N. S., & Marshall, H. L. 2003, ApJ, 590, 432
- Jonker, P. G., & Nelemans, G. 2004, MNRAS, 354, 355
- Kokubun, M., et al. 2007, PASJ, 59, 53
- Kuulkers, E., Homan, J., van der Klis, M., Lewin, W. H. G., & Méndez, M. 2002, A&A, 382, 947
- Lamb, P., & Sanford, P. W. 1979, MNRAS, 188, 555
- Lightman, A. P., & Eardley, D. M. 1974, ApJ, 187, L1
- Lin, D., Remillard, R. A., & Homan, J. 2007, ApJ, 667, 1073
- Lin, D., Remillard, R. A., & Homan, J. 2010, ApJ, 719, 1350
- Lyu, M., Méndez, M., Sanna, A., et al. 2014, MNRAS, 440, 1165
- Maccarone, T. J. 2003, A&A, 409, 697
- Makishima, K. 2007, Progress of Theoretical Physics Supplement, 169, 214
- Makishima, K. 2014, 40th COSPAR Scientific Assembly. Held 2-10 August 2014, in Moscow, Russia, Abstract E1.1-1-14., 40, 1953
- Matsuoka, M., & Asai, K. 2013, PASJ, 65, 26
- Meyer-Hofmeister, E., Liu, B. F., & Meyer, F. 2005, A&A, 432, 181
- Mitsuda, K., et al. 1984, PASJ, 36, 741
- Mitsuda, K., Inoue, H., Nakamura, N., & Tanaka, Y. 1989, PASJ, 41, 97



- Mitsuda, K., et al. 2007, PASJ, 59, 1
- Miyamoto, S., Kitamoto, S., Hayashida, K., & Egoshi, W. 1995, ApJ, 442, L13
- Nakamura, N., Dotani, T., Inoue, H., et al. 1989, PASJ, 41, 617
- Ono, K., Sakurai, S., Zhang, Z., Nakazawa, K., & Makishima, K. 2016, PASJ, doi: 10.1093/pasj/psw003
- Orosz, J. A., & Kuulkers, E. 1999, MNRAS, 305, 132
- Parmar, A. N., White, N. E., Giommi, P., & Gottwald, M. 1986, ApJ, 308, 199
- Poutanen, J., & Svensson, R. 1996, ApJ, 470, 249
- Reeves, J., Done, C., Pounds, K., et al. 2008, MNRAS, 385, L108
- Sakurai, S., Yamada, S., Torii, S., Noda, H., Nakazawa, K., Makishima, K., & Takahashi, H. 2012, PASJ, 64, 72
- Sakurai, S., Torii, S., Noda, H., et al. 2014, PASJ, 66, 10
- Sakurai, S. 2015, PhD thesis ...
- Sasano, M., Makishima, K., Sakurai, S., Zhang, Z., & Enoto, T. 2014, PASJ, 66, 35
- Savolainen, P., Hannikainen, D. C., Vilhu, O., et al. 2009, MNRAS, 393, 569
- Sidoli, L., Parmar, A. N., & Oosterbroek, T. 2005, A&A, 429, 291
- Sunyaev, R. A., & Titarchuk, L. G. 1980, A&A, 86, 121
- Tarana, A., Bazzano, A., Ubertini, P., et al. 2006, A&A, 448, 335
- Tarana, A., Bazzano, A., & Ubertini, P. 2008, ApJ, 688, 1295
- Tarana, A., Belloni, T., Bazzano, A., Méndez, M., & Ubertini, P. 2011, MNRAS, 416, 873
- White, N. E., & Mason, K. O. 1985, Space Sci. Rev., 40, 167
- White, N. E., & Swank, J. H. 1982, ApJ, 253, L61
- Wolff, M. T., Becker, P. A., Ray, P. S., & Wood, K. S. 2005, ApJ, 632, 1099
- Yamada, S., et al. 2012, PASJ, 64, 53
- Zdziarski, A. A., Johnson, W. N., & Magdziarz, P. 1996, MNRAS, 283, 193

Zhang, Z., et al. 2014, PASJ, submitted

Życki, P. T., Done, C., & Smith, D. A. 1999, MNRAS, 309, 561

Table 1: Results of the model fittings to the 0.6 – 55 keV *Suzaku* spectra of the persistent emission of EXO 0748–676.<sup>a</sup>

Component	Parameter	Value	
model		single-seed <sup>b</sup>	double-seed <sup>c</sup>
wabs	$N_{\text{H}}(10^{22} \text{ cm}^{-2})$	0.11 (fixed)	0.11 (fixed)
zxipcf	$N_{\text{abs}}(10^{22} \text{ cm}^{-2})$	$0.14^{+0.95}_{-0.09}$	0.38(< 5.85)
	$\log(\xi)$	$2.36^{+0.29}_{-0.26}$	$2.34^{+0.78}_{-0.73}$
	CvrFract	0.59(> 0.14)	0.21(< 0.34)
Al K-edge <sup>d</sup>	optical depth	$0.03 \pm 0.02$	$0.05 \pm 0.02$
gabs <sup>e</sup>	$E$ (keV)	$1.03 \pm 0.02$	$1.03 \pm 0.02$
	line strength ( $10^{-3}$ )	$5.6 \pm 2.0$	$5.0 \pm 2.0$
diskbb	$kT_{\text{in}}$ (keV)	$0.17 \pm 0.01$	$0.14 \pm 0.01$
	$R_{\text{in}}^f$ (km)	$159^{+26}_{-20}$	$284^{+28}_{-14}$
bbody	$kT_{\text{bb}}$ (keV)	0.19(< 0.25)	$0.32^{+0.07}_{-0.09}$
	$R_{\text{bb}}$ (km)	61(> 33)	$23^{+31}_{-9}$
nthcomp	seed component	bbody	diskbb/bbody
	$\Gamma$	$1.76 \pm 0.01$	$5.11^{+4.50}_{-0.86}/1.75 \pm 0.01$
	$kT_{\text{e}}$ (keV)	$13.9^{+3.7}_{-2.0}$	$12.2^{+2.4}_{-1.5}$ (common)
	$\tau$	$4.9^{+0.5}_{-0.7}$	$1.1^{+0.5}_{-0.8}/5.3^{+1.1}_{-0.9}$
	y-parameter	$1.38 \pm 0.02$	$0.13^{+0.06}_{-0.09}/1.39 \pm 0.04$
Fit goodness	$\chi^2_{\nu}(\text{dof})$	1.03 (137)	0.99 (136)

<sup>a</sup>

The 0.6 – 10 keV XIS spectrum and 12 – 55 keV HXD-PIN spectrum are fitted simultaneously. The quoted errors refer to 90% confidence, statistical only.

<sup>b</sup> diskbb+nthcomp[bbody].

<sup>c</sup> nthcomp[diskbb]+nthcomp[bbody], with the two Comptonized components having a common  $kT_{\text{e}}$  but different  $\tau$ .

<sup>d</sup> The edge energy is fixed to 1.56 keV.

<sup>e</sup> The  $1\sigma$  line width is fixed to 20 eV.

<sup>f</sup>  $R_{\text{in}}$  is corrected for the inclination factor  $\sqrt{\cos(i)}$ , assuming  $i = 80^\circ$ .

Table 2:: *Suzaku* observations of normal non-dipping LMXBs.

Name	OBSID	Exp. <sup>a</sup> (ks)	$L_{\text{abs}}^b$ (erg s <sup>-1</sup> )	$H^c$	$D$ (kpc)	Ref. <sup>d</sup>
4U 1608–52	404044010	28.0	$1.4 \times 10^{37}$	$(4.65 \pm 0.04) \times 10^{-3}$	3.6	1
	404044020	25.2	$7.7 \times 10^{36}$	$(5.38 \pm 0.07) \times 10^{-3}$		
	404044030	14.2	$3.3 \times 10^{36}$	$(3.97 \pm 0.04) \times 10^{-2}$		
	404044040	14.5	$1.0 \times 10^{36}$	$(5.19 \pm 0.09) \times 10^{-2}$		
4U 1636–536	401050010	20.3	$6.5 \times 10^{36}$	$(5.18 \pm 0.05) \times 10^{-2}$	5.92	2
	401050020	33.2	$1.1 \times 10^{37}$	$(5.85 \pm 0.08) \times 10^{-3}$		
	401050030	45.2	$8.7 \times 10^{36}$	$(1.64 \pm 0.01) \times 10^{-2}$		
	401050040	26.1	$8.5 \times 10^{36}$	$(6.6 \pm 0.1) \times 10^{-3}$		
	401050050	11.0	$8.6 \times 10^{36}$	$(5.0 \pm 0.1) \times 10^{-3}$		
4U 1705–44	401046010	14.4	$8.1 \times 10^{36}$	$(4.59 \pm 0.05) \times 10^{-2}$	$7.4^{+0.8}_{-1.1}$	3
	401046020	14.7	$1.7 \times 10^{37}$	$(2.46 \pm 0.06) \times 10^{-3}$		
	401046030	16.7	$6.7 \times 10^{36}$	$(2.14 \pm 0.08) \times 10^{-3}$		
	402051010	8.8	$5.7 \times 10^{37}$	$(3.48 \pm 0.06) \times 10^{-3}$		
	402051020	14.8	$3.7 \times 10^{37}$	$(3.44 \pm 0.06) \times 10^{-3}$		
	402051030	19.5	$1.5 \times 10^{37}$	$(4.16 \pm 0.09) \times 10^{-3}$		
	402051040	12.4	$4.0 \times 10^{37}$	$(3.60 \pm 0.06) \times 10^{-3}$		
	406076010	84.5	$4.6 \times 10^{36}$	$(6.10 \pm 0.04) \times 10^{-2}$		
4U 1728–34	405048010	88.3	$5.9 \times 10^{36}$	$(1.77 \pm 0.01) \times 10^{-2}$	5.2	4
4U 1812–12	406008010	49.9	$1.4 \times 10^{36}$	$(1.208 \pm 0.009) \times 10^{-1}$	4	5
Aql X–1	402053010	12.5	$9.6 \times 10^{36}$	$(2.06 \pm 0.08) \times 10^{-3}$	$5.2 \pm 0.7$	6
	402053020	11.2	$1.9 \times 10^{36}$	$(7.2 \pm 0.1) \times 10^{-2}$		
	402053030	16.1	$2.3 \times 10^{36}$	$(6.6 \pm 0.1) \times 10^{-2}$		
	402053040	16.3	$1.8 \times 10^{36}$	$(7.1 \pm 0.1) \times 10^{-2}$		
	402053050	15.9	$3.5 \times 10^{35}$	$(7.1 \pm 0.3) \times 10^{-2}$		
	402053060	19.8	$9.1 \times 10^{33}$	$(6 \pm 2) \times 10^{-2}$		
	402053070	13.4	$1.1 \times 10^{34}$	$(1.2 \pm 0.3) \times 10^{-1}$		
	406010010	32.8	$1.0 \times 10^{37}$	$(6.89 \pm 0.03) \times 10^{-2}$		
	406010020	35.2	$(2.7\text{--}3.7) \times 10^{37}$	0.12 – 0.008		
	406010030	34.0	$4.7 \times 10^{37}$	$(3.08 \pm 0.02) \times 10^{-3}$		
Cen X–4	403057010	124.0	$5.1 \times 10^{31}$	$(9 \pm 3) \times 10^{-2}$	$1.2 \pm 0.3$	7
Cyg X–2	401049010	34.5	$5.7 \times 10^{37}$	$(2.15 \pm 0.02) \times 10^{-3}$	7.28	8
	403063010	81.9	$5.9 \times 10^{37}$	$(6.50 \pm 0.04) \times 10^{-3}$		

Table 2:: continued.

Name	OBSID	Exp. <sup>a</sup> (ks)	$L_{\text{abs}}^b$ (erg s <sup>-1</sup> )	$H^c$	$D$ (kpc)	Ref. <sup>d</sup>
GS 1826–238	404007010	82.0	$1.1 \times 10^{37}$	$(1.038 \pm 0.004) \times 10^{-1}$	$7_{-3}^{+1}$	9
GX 17+2	402050010	15.0	$1.5 \times 10^{38}$	$(6.23 \pm 0.05) \times 10^{-3}$	9.8	10
	402050020	17.7	$7.2 \times 10^{37}$	$(1.92 \pm 0.01) \times 10^{-2}$		
	406070010	81.1	$1.8 \times 10^{38}$	$(6.28 \pm 0.02) \times 10^{-3}$		
GX 340+0	403060010	80.3	$8.5 \times 10^{37}$	$(9.05 \pm 0.04) \times 10^{-3}$	$11 \pm 3$	11
GX 349+2	400003010	18.7	$4.5 \times 10^{37}$	$(3.82 \pm 0.03) \times 10^{-3}$	5	12
	400003020	23.9	$1.9 \times 10^{37}$	$(2.94 \pm 0.02) \times 10^{-2}$		
GX 9+9	404071010	57.6	$7.6 \times 10^{37}$	$(4.57 \pm 0.04) \times 10^{-3}$	10	13
LMC X–2	401012010	69.0	$1.5 \times 10^{38}$	$(1.01 \pm 0.05) \times 10^{-3}$	50	14
Ser X–1	401048010	15.3	$4.8 \times 10^{37}$	$(2.82 \pm 0.03) \times 10^{-3}$	8.4	12
SLX 1737–282	503103010	29.0	$3.5 \times 10^{35}$	$(8.2 \pm 0.4) \times 10^{-2}$	5 – 8	15

a

Net exposure per XIS sensor.

<sup>b</sup> Absorbed luminosity in 0.8 – 60 keV. For SLX 1737–282, the 6.5 kpc median value of the source distance was used.

<sup>c</sup> Hardness of the 20 – 40 keV HXD-PIN signal rates to the 5 – 10 keV XIS-FI signal rates.

<sup>d</sup> References from which the source distance is quoted: <sup>1</sup>Nakamura et al. (1989), <sup>2</sup>Cornelisse et al. (2003), <sup>3</sup>Haberl & Titarchuk (1995), <sup>4</sup>Galloway et al. (2003), <sup>5</sup>Cocchi et al. (2000), <sup>6</sup>Jonker & Nelemans (2004), <sup>7</sup>Chevalier et al. (1989), <sup>8</sup>Orosz & Kuulkers (1999), <sup>9</sup>Barret et al. (2000), <sup>10</sup>Kuulkers et al. (2002), <sup>11</sup>Fender & Hendry (2000), <sup>12</sup>Christian & Swank (1997), <sup>13</sup>Savolainen et al. (2009), <sup>14</sup>Feast (1999), <sup>15</sup>in’t Zand et al. (2002).

Table 3: The model fittings to the broadband *Suzaku* continuum spectra of the LHS LMXBs.

Name	ObsID	Model	$L_X^a$ ( $\text{erg s}^{-1}/L_{\text{edd}}$ )	$N_{\text{H}}$ ( $10^{22} \text{ cm}^{-2}$ )	$kT_{\text{in}}^b$ (keV)	$R_{\text{in}}^b$ (km)	$kT_{\text{bb}}$ (keV)	$R_{\text{bb}}$ (km)	$kT_e$ (keV)	$\tau$	$y$	$\chi^2_{\nu}(\text{dof})$
(C1) Single-seed Comptonization model without detectable disk												
Aql X-1	402053050	compPS[bbody]	$6.48 \times 10^{35}/3 \times 10^{-3}$	0.36(fixed)	—	—	$0.40 \pm 0.01$	$7 \pm 1$	$146 \pm 10$	$0.49 \pm 0.02$	$0.67 \pm 0.06$	1.05(179)
	402053060	compPS[bbody]	$1.63 \times 10^{34}/8 \times 10^{-5}$	0.36(fixed)	—	—	$0.27 \pm 0.01$	$3 \pm 1$	$170^{+50}_{-40}$	$0.19^{+0.04}_{-0.03}$	$0.27^{+0.08}_{-0.10}$	0.94(134)
	402053070	compPS[bbody]	$3.34 \times 10^{34}/1.6 \times 10^{-4}$	0.36(fixed)	—	—	$0.27 \pm 0.01$	$3 \pm 1$	$400^{+250}_{-130}$	$0.16^{+0.03}_{-0.02}$	$0.53^{+0.34}_{-0.27}$	0.81(134)
SLX 1737-282	503103010	compPS[bbody]	$6.14 \times 10^{35}/3 \times 10^{-3}$	$1.4 \pm 0.1$	—	—	$0.50 \pm 0.04$	$4 \pm 1$	$140 \pm 30$	$0.52^{+0.07}_{-0.05}$	$0.67^{+0.27}_{-0.20}$	1.02(352)
Cen X-4	403057010	compPS[bbody]	$1.08 \times 10^{32}/5 \times 10^{-7}$	0.05(fixed)	—	—	$0.19 \pm 0.01$	$0.5 \pm 0.2$	$400^{+700}_{-200}$	$0.11^{+0.07}_{-0.02}$	$0.36^{+0.42}_{-0.21}$	1.14(39)
(C2) Single-seed Comptonization model with detectable disk												
Aql X-1	402053020	diskbb+compPS[bbody]	$3.07 \times 10^{36}/1.5 \times 10^{-2}$	0.36(fixed)	$0.28 \pm 0.02$	$23^{+4}_{-3}$	$0.53 \pm 0.02$	$9 \pm 1$	$64 \pm 6$	$0.81 \pm 0.04$	$0.51 \pm 0.08$	1.15(363)
	402053030	diskbb+compPS[bbody]	$3.57 \times 10^{36}/1.7 \times 10^{-2}$	0.36(fixed)	$0.28 \pm 0.02$	$27 \pm 4$	$0.52 \pm 0.02$	$10 \pm 1$	$51 \pm 5$	$0.98^{+0.06}_{-0.05}$	$0.51^{+0.09}_{-0.08}$	1.09(363)
	402053040	diskbb+compPS[bbody]	$2.75 \times 10^{36}/1.2 \times 10^{-2}$	0.36(fixed)	$0.28^{+0.07}_{-0.05}$	$15^{+7}_{-5}$	$0.51 \pm 0.02$	$9 \pm 1$	$64 \pm 6$	$0.81 \pm 0.04$	$0.51 \pm 0.08$	1.16(363)
4U 1608-52	404044030	diskbb+nthcomp[bbody]	$6.47 \times 10^{36}/3.1 \times 10^{-2}$	$1.10 \pm 0.04$	$0.55^{+0.03}_{-0.04}$	$16 \pm 1$	$0.9 \pm 0.1$	$4 \pm 1$	$22^{+78}_{-8}$	$2.5^{+0.8}_{-1.7}$	$0.75^{+0.05}_{-0.06}$	1.24(376)
	404044040	diskbb+compPS[bbody]	$1.84 \times 10^{36}/8.8 \times 10^{-3}$	$1.1 \pm 0.1$	$0.32^{+0.1}_{-0.06}$	$17^{+13}_{-7}$	$0.47^{+0.07}_{-0.04}$	$8^{+1}_{-2}$	$54^{+8}_{-13}$	$1.0^{+0.3}_{-0.1}$	$0.56^{+0.34}_{-0.19}$	1.20(331)
4U 1636-536	401050010	diskbb+nthcomp[bbody]	$9.71 \times 10^{36}/4.6 \times 10^{-2}$	$0.19 \pm 0.01$	$0.55 \pm 0.02$	$14 \pm 1$	$0.86 \pm 0.05$	$6 \pm 1$	$20^{+5}_{-3}$	$3.2^{+0.4}_{-0.3}$	$0.96 \pm 0.02$	1.15(380)
4U 1812-12	406008010	diskbb+compPS[bbody]	$4.63 \times 10^{36}/2.2 \times 10^{-2}$	$2.0 \pm 0.2$	$0.24^{+0.05}_{-0.03}$	$50^{+40}_{-30}$	$0.51 \pm 0.02$	$10 \pm 1$	$83^{+8}_{-9}$	$0.80^{+0.10}_{-0.08}$	$0.65^{+0.17}_{-0.14}$	1.13(331)
(C3) Double-seed Comptonization model with common corona												
Aql X-1	406010010	nthcomp[diskbb+bbody]	$1.49 \times 10^{37}/7.1 \times 10^{-2}$	0.36(fixed)	$0.27^{+0.07}_{-0.06}$	$40^{+24}_{-14}$	$0.62 \pm 0.03$	$11 \pm 1$	$21 \pm 1$	$3.60 \pm 0.07$	$1.24 \pm 0.02$	1.02(330)
4U 1705-44	401046010	nthcomp[diskbb+bbody]	$1.13 \times 10^{37}/5.4 \times 10^{-2}$	$1.6 \pm 0.1$	$0.13(< 0.36)$	$68(> 5)$	$0.62 \pm 0.01$	$11 \pm 1$	$23^{+4}_{-3}$	$3.4^{+0.3}_{-0.2}$	$1.24 \pm 0.02$	1.10(326)
	406076010	nthcomp[diskbb+bbody]	$6.84 \times 10^{36}/3.3 \times 10^{-2}$	1.6(fixed)	0.13(fixed)	$85 \pm 5$	$0.59 \pm 0.01$	$10 \pm 1$	$19^{+4}_{-2}$	$3.7^{+0.4}_{-0.2}$	$1.15 \pm 0.02$	1.06(314)
GS 1826-238 <sup>c</sup>	404007010	dkbbfth+nthcomp[bbody]	$1.5 \times 10^{37}/7 \times 10^{-2}$	0.28(fixed)	$0.42^{+0.08}_{-0.20}$	$> 21$	$0.63^{+0.01}_{-0.02}$	$11.9 \pm 0.3$	$> 50$	$< 1.9$	$1.21^{+0.08}_{-0.03}$	1.01(291)

<sup>a</sup> The unabsorbed bolometric luminosity derived from the best-fit modeling. The eddington luminosity  $L_{\text{edd}}$  is  $2.1 \times 10^{38} \text{ erg s}^{-1}$  for the canonical NS mass of  $1.4M_{\odot}$ .

<sup>b</sup>  $R_{\text{in}}$  is corrected for the inclination factor  $\sqrt{\cos(i)}$ , assuming  $i = 45^\circ$ .

<sup>c</sup> Results of this source are quoted from Ono et al. (2016), in which a partially Comptonized disk blackbody model dkbbfth is applied.



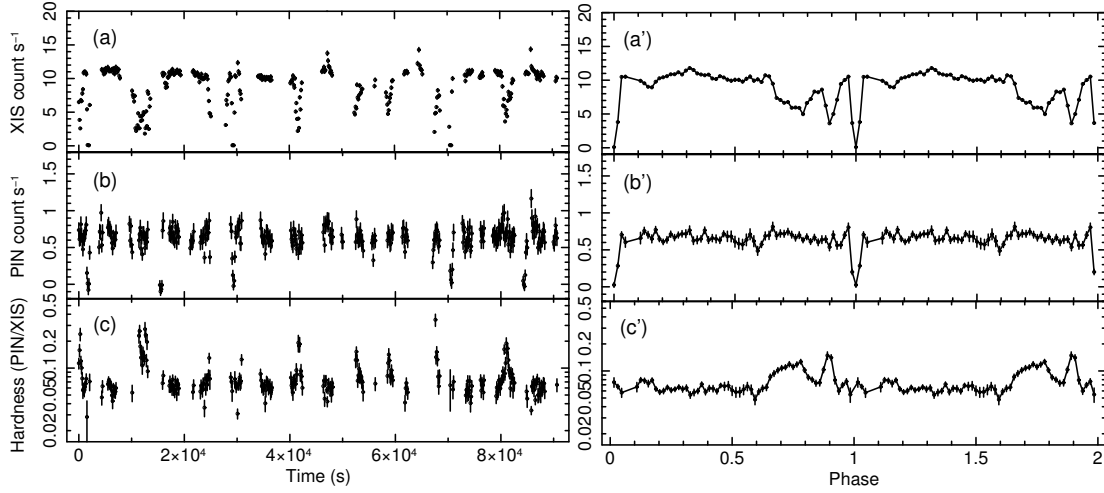


Fig. 1.— *Suzaku* light curves and hardness ratio of EXO 0748–676 with a time binsize of 128 s (left panels), and those folded on  $P_{\text{orb}} = 13766.8$  s with 64 phase bins per period after excluding the bursts (right panels), where phase 0 (= 1) refers to 06:12:03 of 2007 December 25. Panels (a) and (a') show the background-subtracted 0.6 – 10 keV XIS light curves (averaged between XIS 0 and XIS 3). Panels (b) and (b') show NXB-subtracted 12 – 55 keV HXD-PIN light curves, including the CXB contribution by  $\sim 0.02$  cts  $\text{s}^{-1}$ . The HXD-PIN vs. XIS hardness ratios are shown in (c) and (c').

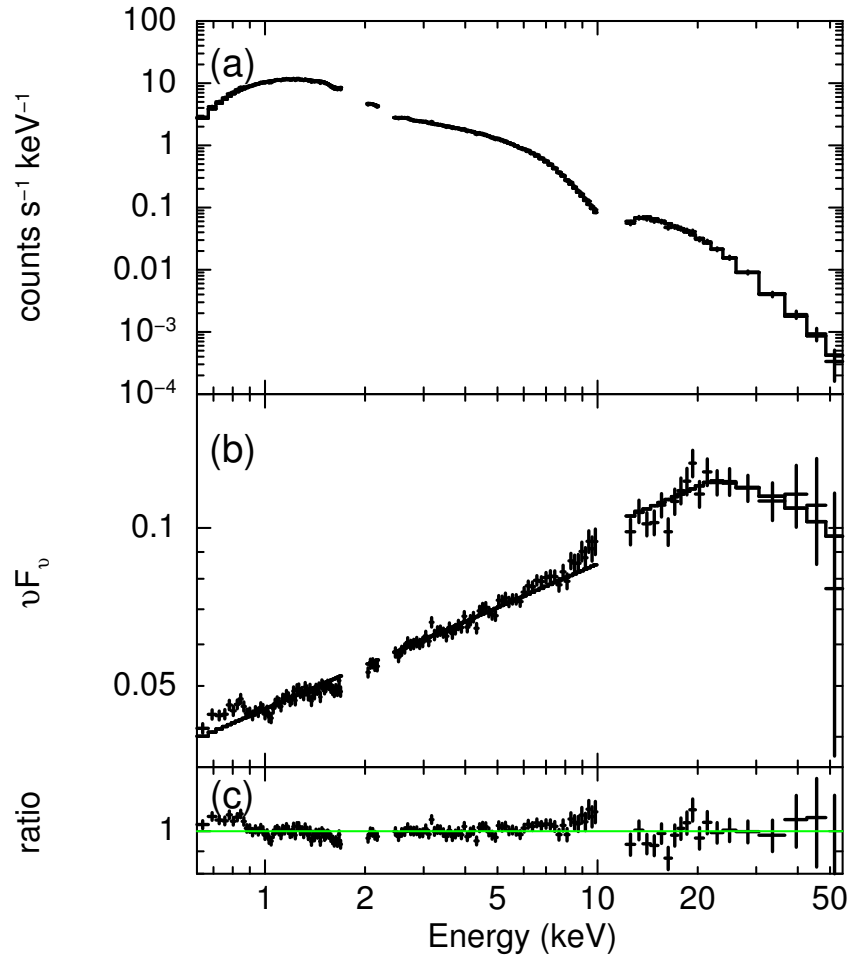


Fig. 2.— The persistent *Suzaku* spectrum of EXO 0748–676 and its approximation by an empirical model `highecut*powerlaw`. (a) The count spectrum and the best-fit model. (b) The deconvolved  $\nu F_\nu$  plot and the fitted empirical model. (c) The ratio of the spectrum to the model.

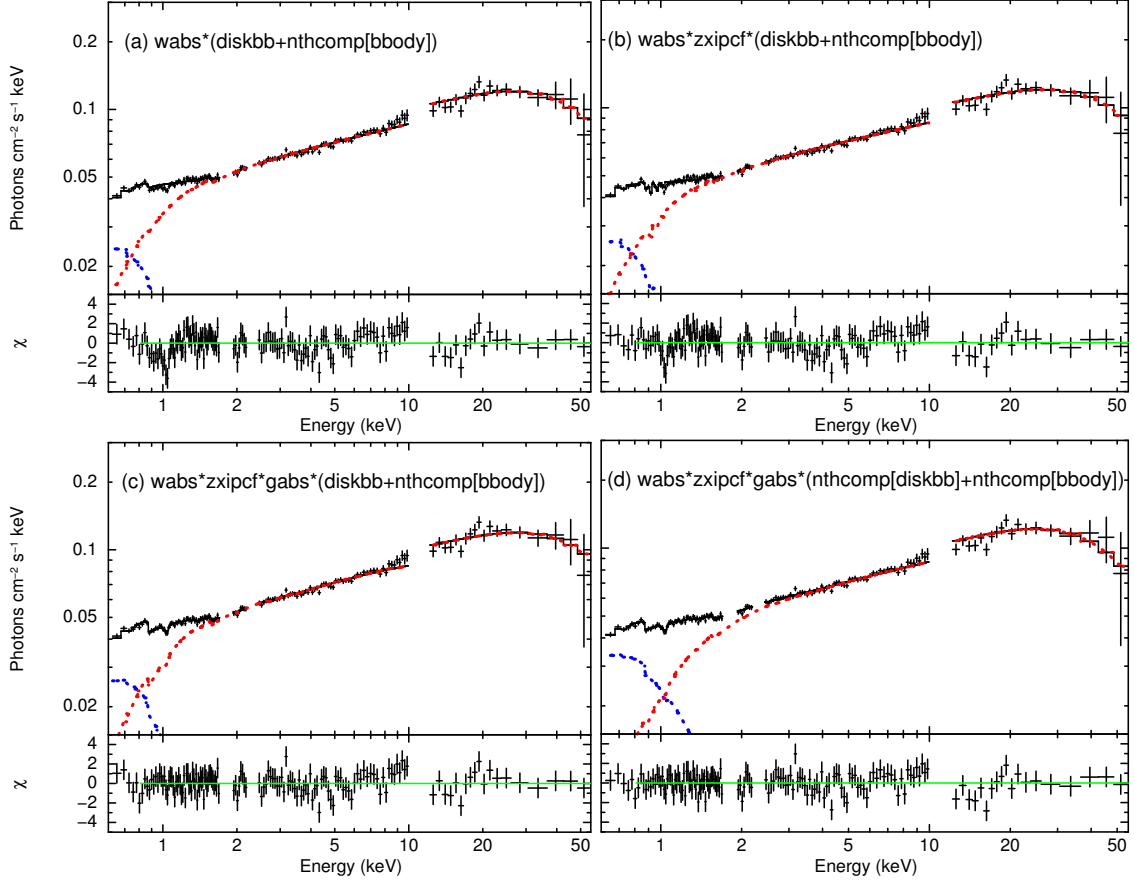


Fig. 3.— The deconvolved  $\nu F_\nu$  spectrum of EXO 0748–676 and the results of fitting with physical models. (a) Fit with a diskbb (soft component) plus nthcomp[bbody] (hard component) model with Galactic absorption, and its residuals. (b) Improvement of panel (a) by multiplying a partial ionized absorber zxipcf (Reeves et al. 2008). (c) Improvement of panel (b) by including a Gaussian absorption feature at  $\sim 1$  keV. (d) A double-seed Comptonization solution employing an nthcomp[diskbb] (soft component) plus nthcomp[bbody] (hard component) model. The two Comptonized components have a common electron temperature but different optical depths.

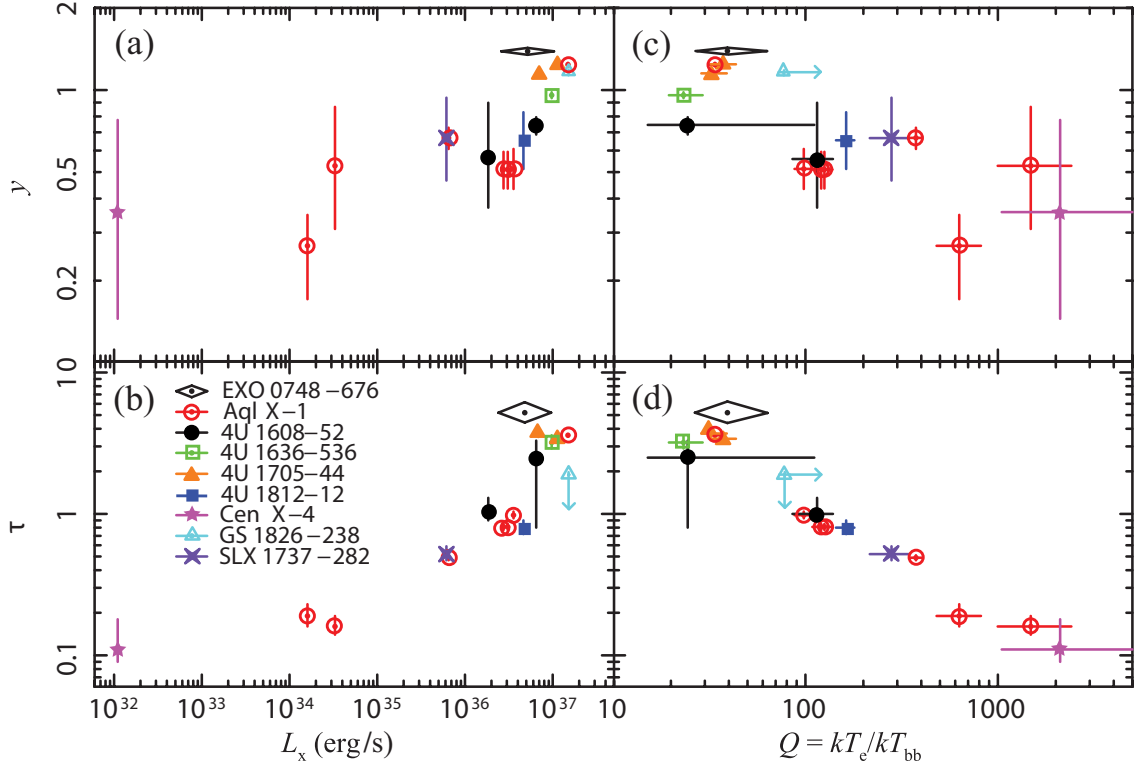


Fig. 4.— The  $L_X$ - $y$  (panel a) and  $L_X$ - $\tau$  (panel b) plots for the Comptonization of the NS blackbodies in the LHS LMXBs given in table 3. Panels (c) and (d) give  $Q$ - $y$  and  $Q$ - $\tau$  plots, respectively.